ARTICLE

https://doi.org/10.1038/s41586-019-1348-3

Hyperbolic lattices in circuit quantum electrodynamics

Alicia J. Kollár[1,2,3]*, Mattias Fitzpatrick[1] & Andrew A. Houck[1]

After two decades of development, cavity quantum electrodynamics with superconducting circuits has emerged as a rich platform for quantum computation and simulation. Lattices of coplanar waveguide resonators constitute artificial materials for microwave photons, in which interactions between photons can be incorporateded either through the use of nonlinear resonator materials or through coupling between qubits and resonators. Here we make use of the previously overlooked property that these lattice sites are deformable and permit tight-binding lattices that are unattainable even in solid-state systems. We show that networks of coplanar waveguide resonators can create a class of materials that constitute lattices in an effective hyperbolic space with constant negative curvature. We present numerical simulations of hyperbolic analogues of the kagome lattice that show unusual densities of states in which a macroscopic number of degenerate eigenstates comprise a spectrally isolated flat band. We present a proof-of-principle experimental realization of one such lattice. This paper represents a step towards on-chip quantum simulation of materials science and interacting particles in curved space.

Euclidean space-time is the familiar geometry of non-relativistic physics. Its spatial dimensions are geometrically flat. Within this paradigm, Newtonian gravity is completely described by a scalar potential. However, this is insufficient to describe gravitational radiation or strong gravitational fields. These situations require general relativity in which gravity appears as variations in the metric of space-time. The resulting mass-dependent curvature modifies the properties of parallel lines and geodesics, and even though particles move along the shortest paths between points, they no longer move along the intuitive straight lines of Euclidean geometry. The equations of motion must now be formulated in terms of the metric tensor, which can no longer be written in a position-independent way. The behaviour of classical astrophysical objects in this mass- and position-dependent metric has been studied and simulated extensively, but a consistent formulation of both gravitation and quantum mechanics remains elusive. Therefore, a tabletop simulator that naturally incorporates curvature and non-classical degrees of freedom is of considerable interest.

Positive spatial curvature is naturally realized in the laboratory as the surface of a sphere. In contrast, a surface with constant negative (hyperbolic) spatial curvature[1] cannot be realized in Euclidean space without distortion. This lack of an isometric embedding makes hyperbolic space much more difficult to attain. Previous experimental simulations of particles in negatively curved space have been restricted to hyperbolic metamaterials in which the dielectric constant is varied to reproduce the effects of a curved metric[2–8]. However, these experiments are purely classical and only weakly interacting. Analogues of event horizons and Hawking radiation[9] have been studied both experimentally and theoretically using acoustic waves[9,10], ultrashort optical pulses[11], Bose–Einstein condensates[12,13] and exciton-polariton condensates[14]. Methods have also been proposed for realizing the Dirac equation in curved space-times by using ion traps[15,16], optical waveguides[17], and optical lattices with position-dependent hopping and non-Abelian artificial gauge fields[18].

Expanding on previous work that realized Euclidean lattice models using the techniques of circuit quantum electrodynamics (QED) and interconnected networks of superconducting microwave resonators[19–23], we present a scheme to generate photonic materials that constitute periodic lattices in the two-dimensional (2D) hyperbolic plane[1,24]. Classical photon–photon interactions can be added by incorporating nonlinear materials into the resonators, and quantum mechanical interactions by introducing qubits[19,21,25,26]. The strongly non-classical properties of superconducting qubits and the large qubit–photon coupling rates available will allow circuit QED hyperbolic materials to access a new regime of simulation of interacting quantum mechanics in curved space. Additionally, these systems realize much stronger curvatures than previously possible, with lattice spacings in excess of approximately 0.5 times the curvature length.

Beyond their natural connection to general relativity, hyperbolic lattices also have important applications in mathematics and computer science. Classification of these lattices and the study of their spectral properties relate to open problems in representation theory of non-commutative groups, graph theory, random walks and automorphic forms[27–33]. Computer scientists often study hyperbolic networks because these have several useful qualities for robust and efficient communication. For example, trees, which are naturally hyperbolic, are highly efficient at connecting a large number of nodes to a few central servers, and in fact the connectivity of the internet is a hyperbolic map[34,35]. Additionally, there exist classes of hyperbolic lattices that, unlike Euclidean lattices, cannot be split in half by the removal of a small number of nodes[36]. They therefore arise frequently in the study of how to fortify a communication network against hostile tampering. This enhanced connectivity also leads to lower-overhead logical-qubit encoding in surface codes[37,38].

Here we will concentrate on a set of examples that are hyperbolic generalizations of the kagome lattice. We present numerical studies of their non-interacting band structures, which display highly unusual features, in particular a spectrally isolated degenerate flat band. In addition, we present experimental measurements of a proof-of-principle device that realizes a finite section of one of these lattices, a kagome lattice made with heptagons instead of hexagons.

[1]Department of Electrical Engineering, Princeton University, Princeton, NJ, USA. [2]Princeton Center for Complex Materials, Princeton University, Princeton, NJ, USA. [3]Joint Quantum Institute and Department of Physics, University of Maryland, College Park, MD, USA. *e-mail: akollar@umd.edu

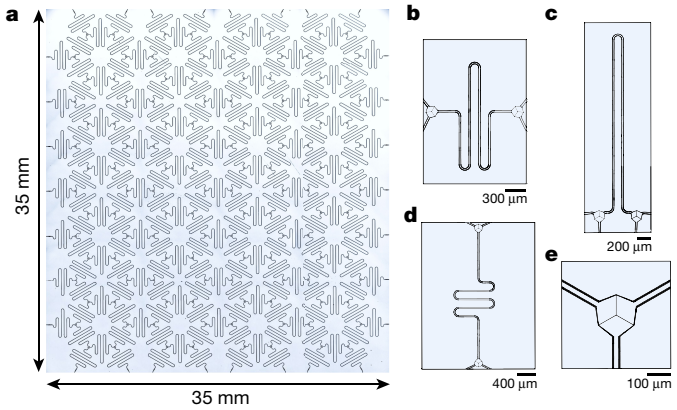

Fig. 1 | Circuit QED lattices. a, Picture of a Euclidean lattice of CPW microwave resonators, modified from ref. [19]. **b**–**d**, Three mathematically identical resonators with different shapes but the same resonance frequencies and hopping rates. Scale bars: **b**, 300 μm; **c**, 200 μm; **d**, 400 μm. **e**, Close-up of a capacitive coupler like the ones used in **a**–**d** to connect three resonators together. Scale bar, 100 μm. The effective hopping rate at this junction is set by the capacitance between the three arrow-shaped centre pins.

Circuit QED lattices

Circuit QED is a solid-state implementation of cavity QED in which superconducting qubits are coupled to microwave resonators[20,39–41]. Strong coupling is readily achievable, and unlike atoms, qubits are lithographically defined, so strong qubit–resonator coupling can be maintained indefinitely. This, coupled with the ease of performing high-fidelity gate operations and relatively long coherence times, makes superconducting qubits a promising candidate for universal digital quantum computation. However, a digital, gate-based architecture is not the only useful one. Pattern recognition and machine learning routinely use architectures based on massively interconnected neural networks. Regular networks map naturally to lattice-based physics problems and are therefore a convenient platform for quantum simulation of many-body physics[19,22].

Creating this type of architecture by connecting many resonators together results in artificial photonic materials, which have been realized using both three-dimensional stub resonators[20,41] and the 2D coplanar waveguide (CPW) resonators[19,21,22,39] that we use here. An example lattice is shown in Fig. 1a. In the absence of interactions, CPW lattices are well described by a tight-binding model, whose Hamiltonian can be written in the following form (with $\hbar = 1$):

$$H_{\mathrm{TB}} = \omega_0 \sum_i a_i^\dagger a_i - t \sum_{<i,j>} (a_i^\dagger a_j + a_j^\dagger a_i) \qquad (1)$$

where the first sum encodes the on-site energy ω_0, and the second describes hopping between nearest neighbours $\langle i,j \rangle$ with a characteristic rate $t < 0$ (refs [19,22]). The geometry of the lattice is encoded entirely in the structure of this last sum. Consider the example of a 2D square lattice. A colour map of the potential is shown in Fig. 2a. The tight-binding approximation is equivalent to replacing this continuum model with a graph-based one such as that shown in Fig. 2b. Each on-site wavefunction is replaced with a single complex amplitude. The graph has one edge for each allowed hopping transition, weighted by the corresponding hopping rates. Once this assignment has been made, the tight-binding model is fully specified and, in fact, independent of how the graph is drawn. For example, the graph shown in Fig. 2c is identical to that in Fig. 2b despite the fact that it appears disordered.

Such a deformation is challenging in an atomic quantum simulator because the effective t is determined by the physical distance between atoms. However, the situation is quite different for CPW lattices. In this case, an individual site is a naturally one-dimensional (1D) object whose connections are determined by coupling capacitors at its end points. Like a coaxial cable, a CPW resonator can be bent, and as long as the length of the resonator is fixed, its properties in the tight-binding model are unchanged. Thus, despite the differences in their physical layout, the resonators in Fig. 1b–d are identical. Therefore, provided that the coupling capacitors are unchanged and the resonators can be deformed sufficiently to maintain constant total length, the tight-binding model is unchanged by moving the resonators or the locations of the couplers. It is this flexibility that makes it possible to construct curved-space lattices on flat, Euclidean substrates.

Hyperbolic lattices

Crystallography deals with periodic lattices consisting of a unit cell, possibly with more than one site, and a tiling of that unit cell that fills all of space with no gaps and no overlaps[42]. Geometry therefore strongly constrains the set of all possible unit cells. However, hyperbolic and spherical polygons have larger and smaller internal angles than their Euclidean counterparts, respectively (see Fig. 3). Therefore the set of allowed lattices is different in curved spaces[24]. To see this more clearly, we will adopt a non-standard approach to crystallography that generalizes to curved space more readily than the usual description. We will describe each lattice as a tiling of the plane with polygons such that each lattice site is at a vertex of the tiling, and two vertices are connected by an edge if they are nearest neighbours in the lattice. The tiling will consist of only a few distinct plaquettes, or tiles, and the geometry of the lattice can be classified in terms of the set of tiles and their tiling rule. For example, graphene will be described as a tiling of regular hexagons such that three of them touch at every vertex, as shown in Fig. 3a. Lattices in curved spaces come from tile configurations that do not properly fill space, according to the Euclidean sense. Examples of such tilings are shown in Fig. 3d–i.

To produce an effectively curved lattice in a flat quantum simulator, the tiling must be stretched or distorted into the flat plane, without changing the tight-binding model. Schematics of realizing this transformation using CPW resonators are shown for two different lattices in Fig. 3f, i. The vertices of the curved tiling no longer appear in a highly regular pattern in the physical circuit, but the meanders in the resonators have been adjusted to compensate for the distortion, and the tight-binding model has been preserved.

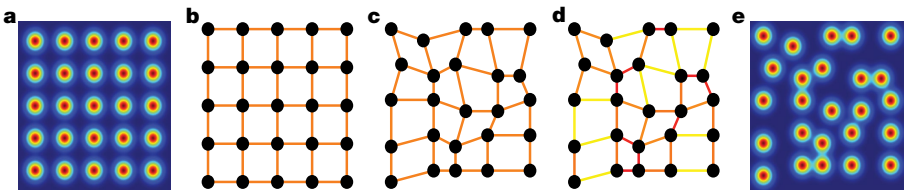

Fig. 2 | The graph is everything. a, Colour plot of the lattice potential of a regular 2D square lattice. **b**, The corresponding regular tight-binding graph of the potential in **a**. **c**, Alternative drawing of the tight-binding graph in **a**. Despite visible displacement of the nodes, the hopping Hamiltonian is unmodified because the hopping rates, indicated by the colour of the graph edges, are identical to **b**. **d**, New tight-binding graph with the same nodes as **c** but with hopping rates dependent on the distance between the nodes. **e**, Highly disordered lattice potential which gives rise to the tight-binding graph in **d**. In some cases, such as the curved-space lattices shown in Fig. 3d–i, the regular tight-binding graph is impossible to produce in 2D flat space, whereas a mathematically identical but distorted-looking graph such as **c** can be fabricated using CPW resonators. This would not be possible in systems where hopping rates are solely determined by the distance between sites.

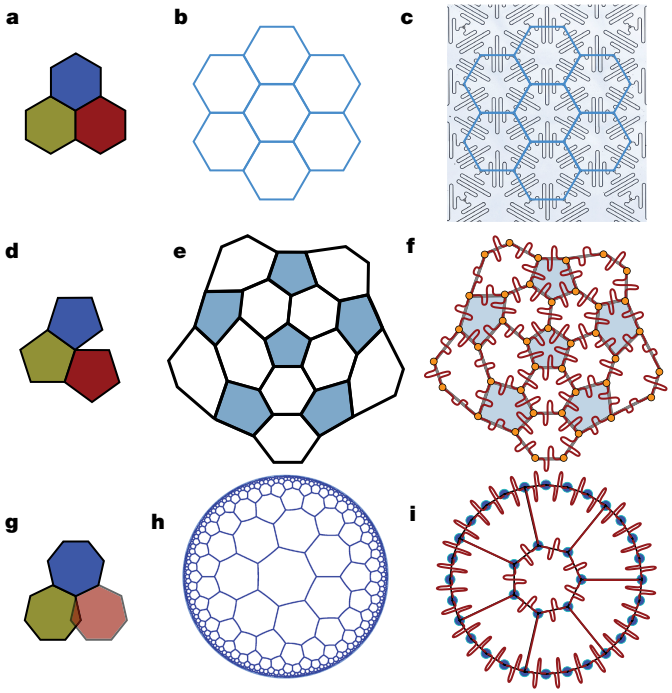

Fig. 3 | Schematic diagram of Euclidean and non-Euclidean lattices in circuit QED. a, One vertex of a successful attempt to tile the Euclidean plane with regular hexagons. **b**, Resulting hexagonal lattice. **c**, Euclidean circuit QED lattice with the resonators laid out in regular hexagons. Because this is a valid Euclidean tiling, the resonator network is highly regular, and all resonators look the same. Photograph modified from ref. [19]. **d**, One vertex of a failed attempt to tile the Euclidean plane with regular pentagons. A gap is left between the tiles, so this tiling is valid only in spherical space (positive curvature). **e**, Projection of a spherical soccer-ball lattice (buckminsterfullerene[42]) into the Euclidean plane. Some tiles must be stretched to cover the missing space. **f**, Schematic of a circuit QED lattice that realizes the soccer-ball tiling. Resonator shapes are modified at different points in the lattice to bridge the stretched distances while preserving the hopping rates and on-site energies. **g**, One vertex of a failed attempt to tile the Euclidean plane with regular heptagons. The tiles overlap, so this tiling is only valid in hyperbolic space (negative curvature). **h**, Conformal projection of a hyperbolic heptagon lattice into the Euclidean plane. **i**, Schematic of a circuit QED lattice that realizes a section of the hyperbolic lattice in **h**. Resonator shapes are modified at different points in the lattice to permit tighter packing while preserving the hopping rates and on-site energies.

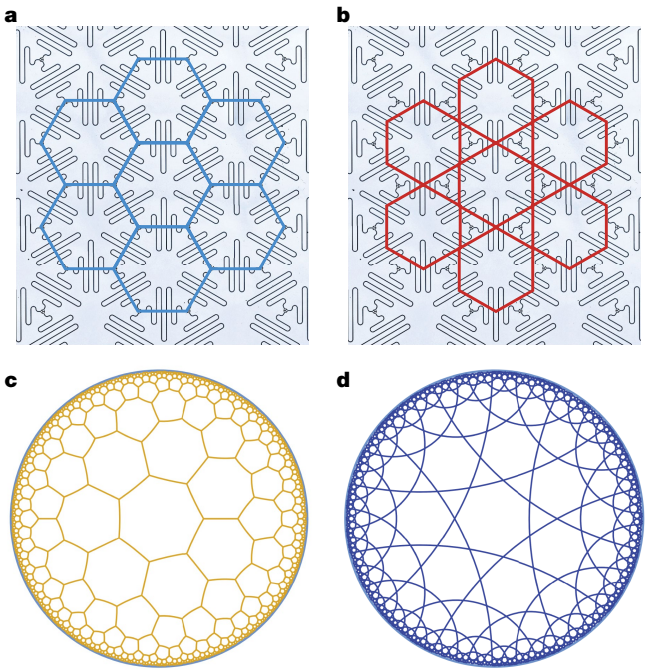

Fig. 4 | Layout graph versus effective kagome graph. a, Microscope image of a Euclidean lattice device (modified from ref. [19]) with the corresponding hexagonal layout graph overlaid in blue. Resonators correspond to edges of the graph and three-way capacitors to vertices. **b**, The same device with the effective, kagome, tight-binding graph overlaid in red. Resonators now correspond to vertices of the graph and non-zero hopping matrix elements to the edges. **c**, **d**, A hyperbolic heptagonal layout graph (**c**) and the resulting effective kagome-like graph (**d**) respectively. Plots in **c** and **d** are visualized in the Poincaré disk model[1].

The constraints on this technique are twofold. First, all resonators must have constant frequency without overlapping on the substrate. Because the turns in a CPW cannot be made arbitrarily tight, the achievable meander density cannot be arbitrarily large. This imposes a limit on the maximum feasible distortion that typically rules out complete spherical tilings, such as buckminsterfullerene[43], or radically curved hyperbolic tilings. However, finite sections of spherical tilings and of many hyperbolic lattices, such as the heptagon version of the kagome lattice (shown in Fig. 4d), are readily achievable.

The second constraint on the set of curved lattices achievable in circuit QED is the fact that the resonators are 1D objects. Consequently, the most natural way to lay them down is to select a tiling and place one resonator on each edge, rather than on each vertex. The effective lattice that then appears in the tight-binding model is the medial lattice, or line graph, of the original layout, where particles live on the centre of the edges and a hopping matrix element exists between effective sites if their edges share an end point. Achievable lattices are therefore those that can be written as the medial of another. Figure 4a, b shows a Euclidean resonator lattice with an overlay of the layout and effective lattices, respectively. The layout lattice is a hexagonal lattice, but the effective lattice is a kagome lattice.

The hyperbolic lattices studied here are natural generalizations of the kagome lattice in which the layout lattice is changed to a hyperbolic version of graphene, such as the heptagonal one shown in Fig. 4c, resulting in an effective kagome-like lattice shown in Fig. 4d. We focus primarily on this heptagon version, which we refer to as the heptagon-kagome lattice, because it belongs to a class of hyperbolic kagome-like lattices whose highly unusual band structures exhibit a spectrally isolated flat band. Additionally, the heptagon-graphene layout lattice has the weakest curvature of all possible tilings of the hyperbolic plane with a single tile, making it particularly easy to fabricate. However, even this weakest curvature is fairly strong. Heptagon-graphene has an inter-site spacing of $0.566R$, and the resulting heptagon-kagome effective lattice has $0.492R$ (ref. [21]), where R is the curvature length of the hyperbolic plane (see Methods for details). Conversely, if we take the inter-site spacing to be that of graphene, then they would have $R = 2.51$ Å and $R = 2.88$ Å, respectively. Plots of other hyperbolic graphene- and kagome-like lattices and their curvatures are shown in Extended Data Fig. 3.

Tight-binding simulations

In Euclidean crystallography, calculation of the tight-binding band structure of a lattice is straightforward once the unit cell, Bravais lattice and hopping rates have been determined. Translation groups in Euclidean space are commutative, so representation theory guarantees that a Bloch-wave ansatz will yield eigenstates and eigenenergies as a function of momentum[42]. In hyperbolic space, however, the discrete translation groups are non-commutative. As a result, there is no natural analogue of a Bravais lattice. In fact, simply writing down the locations of all the lattice sites and the directions of all the bonds is already a non-trivial mathematical problem. The only applicable methods for analysing such lattices are generalized graph-theoretic tools (which only work for tree-like cases) and finite-size exact diagonalization (in order to compute energy spectra or densities of states).

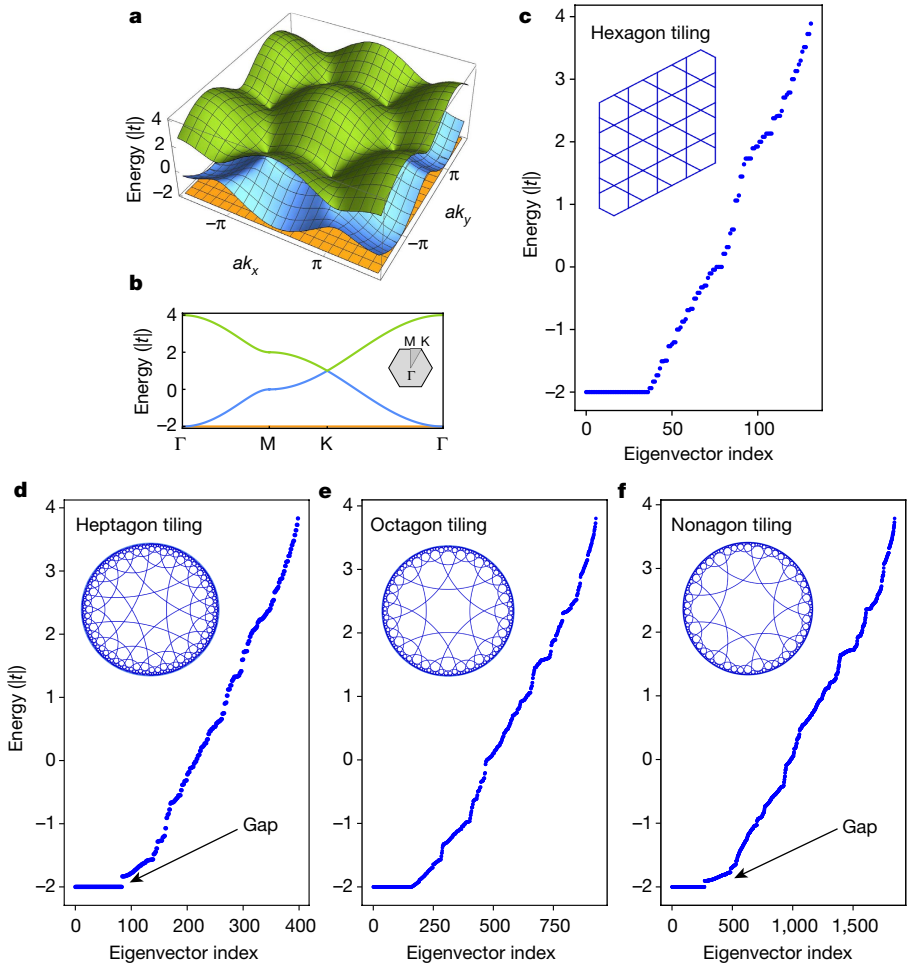

Fig. 5 | Tight-binding simulations. a, Band structure of the kagome lattice for hopping rate $t < 0$ with periodic boundary conditions. The flat band is the lowest energy band at $E = -2|t|$. Two dispersive bands appear in the range $[-2|t|, 4|t|]$ and touch the flat band at the Γ point at $|k| = 0$. Bands are plotted versus the scaled momenta ak_x and ak_y, where a is the interatomic spacing. **b**, Slice through the kagome band structure showing the band touch. These Bloch-theory calculations cannot be generalized to hyperbolic lattices, where the only available technique is numerical diagonalization on finite-sized lattices with hard-wall boundary conditions. **c**, Finite-size numerical eigenenergy spectrum for the kagome lattice. The flat band and the band touch with the dispersive bands are clearly visible, but the structure of the dispersive bands is lost. **d**–**f**, Analogous numerical eigenenergy spectra for hyperbolic versions of the kagome lattice using heptagons, octagons and nonagons, respectively. The flat band is gapped for the case of odd-sided layout polygons, the heptagons and nonagons in **d** and **f**.

We produce finite-size samples by using a cylindrical construction, starting from a single layout polygon and successively adding shells of neighbouring tiles. We compute the effective lattice of this truncated layout and obtain a hopping matrix in a localized, delta-function, basis. Numerical diagonalization yields eigenenergies and eigenstates for each lattice type and simulation size. A sample spectrum for a three-shell piece of the Euclidean kagome lattice is shown in Fig. 5c. It has reduced information compared with the full band-structure calculation in Fig. 5a, b, but the presence of the flat band and accompanying delta-function spike in the density of states at $-2|t|$ is clear. Spectra for the hyperbolic heptagon-, octagon- and nonagon-kagome lattices are shown in Fig. 5d–f. All four spectra share several similar features: a flat band at $-2|t|$ and the remaining bands filling the range from $-2|t|$ to $4|t|$. For the two tilings formed from odd-sided polygons, a spectral gap is visible between the flat band and the remaining eigenstates. This gap is independent of system size and decreases with the number of sides of the layout polygon. The other gaps appear to be finite-size artefacts that close with increasing system size. (See Extended Data Fig. 1 for details.)

Flat bands, like those seen in Fig. 5, are rare in band structures[44,45]. Because the kinetic energy in these bands effectively vanishes, they are ripe for strongly correlated many-body physics and non-perturbative interactions, such as fractional quantum Hall states arising from discrete Landau levels. However, a pure flat-band description is only valid if the interaction strength is smaller than the gap to the nearest dispersive band. This is very much the case with Landau levels where magnetic energies far outweigh tunnelling energies and tight-binding band structure, but otherwise, gapped flat bands are highly unusual. Among Euclidean lattices, there are only a few known examples in which real-space topology of the flat band allows a gap to exist[44,45]. However, there are entire classes of hyperbolic systems that display gapped flat bands, including the $(2n+1)$-gon-kagome lattices, and certain generalizations of trees.

The flat bands arise because of infinite multiplicity of localized eigenstates. In the kagome lattice, the smallest such state consists of a single occupied hexagonal loop with alternating sign of the wavefunction on each site and vanishing occupation elsewhere. This state can easily be generalized to the octagon-kagome lattice, but not to the heptagon or nonagon versions, in which the odd number of sides introduces geometric frustration. In these cases, the flat band still consists of localized states in the form of an alternating closed loop, but it must now extend over two tiles. See Methods and Extended Data Fig. 2g for details. Without a hyperbolic generalization of Bloch theory, the real-space topology techniques used to understand the kagome lattice[44] cannot be extended to hyperbolic flat bands. Understanding the origin and magnitude of the gaps in these cases requires advanced graph-theoretic techniques beyond the scope of this work[46].

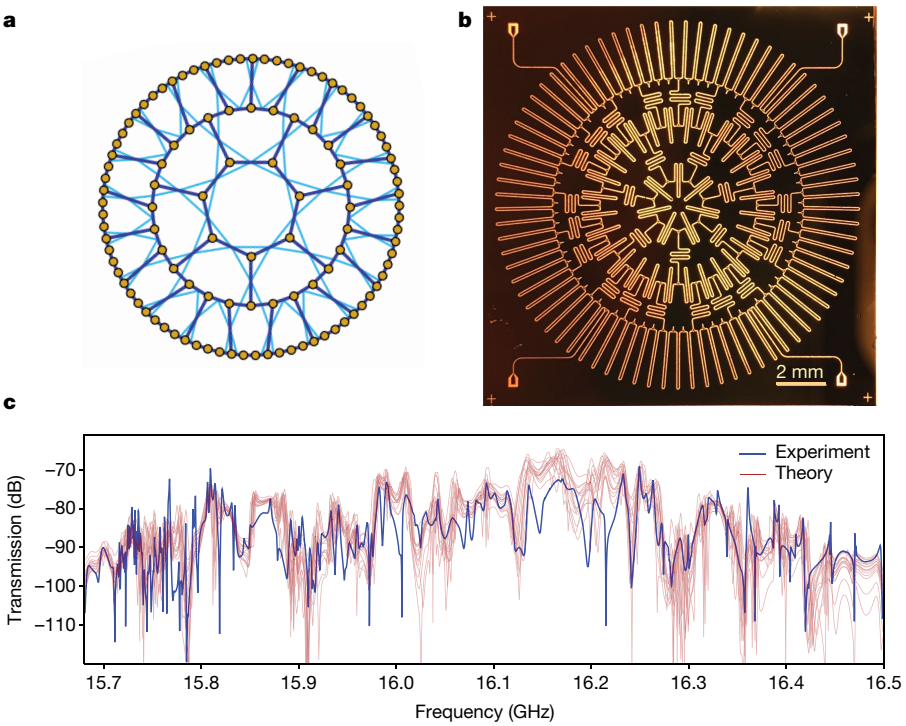

Fig. 6 | The heptagon-kagome device. a, Resonator layout (dark blue) and effective lattice (light blue) for a circuit that realizes two shells of the heptagon-kagome lattice. Orange circles indicate three-way capacitive couplers. **b**, Photograph of a physical device that realizes the layout and effective graphs in **a**. The device consists of 140 CPW resonators with fundamental resonance frequencies of 8 GHz, second harmonic frequencies of 16 GHz and a hopping rate of −136.2 MHz at the second harmonic. Four additional CPW lines at each corner of the device couple microwaves into and out of the device for transmission measurements. Short stubs protruding inward from the outermost three-way couplers are high-frequency $\lambda/4$ resonators, which maintain a consistent loading of the sites in the outer ring, ensuring uniform on-site energies. **c**, Experimental transmission (S_{21}) for the device in **b** is shown in dark blue. The red curves show theoretical transmission for an ensemble of theoretical models including small systematic offsets in the on-site energies and realistic disorder levels, demonstrating reasonable agreement between theory and experiment.

Device measurements

We have constructed a device to realize a finite section of the heptagon-kagome lattice. It consists of one central heptagon and two shells of neighbouring tiles, and is shown schematically in Fig. 6a, where each resonator has been approximated by a single line, and the lengths have not been held fixed. The resonators are 7.5 mm long with a fundamental resonance frequency of 8 GHz and a second harmonic of 16 GHz. The second harmonic of this device realizes the heptagon-kagome lattice with a hopping rate of −136.2 MHz. (The fundamental modes of the device obey a different tight-binding model owing to the asymmetry of the mode function within each resonator[22]. See the Methods for details.)

To minimize parasitic systematic frequency differences between resonator geometries, each resonator type was fabricated individually, and the corresponding resonant frequencies were measured. Commercial microwave simulation packages were unable to achieve the required level of absolute or relative accuracy, so the resonator lengths were then fine-tuned empirically to remove the residual offsets at the level of 30 MHz. For the device shown in Fig. 6b, the average difference between the fundamental frequencies of resonators with different shapes is approximately 0.13% (10 MHz), limited by intrinsic reproducibility within a fabrication run[23] and wire-bonding or parasitic capacitances sensitive to variations between fabrication runs. Each individual shape has a fabrication-induced reproducibility of 0.036% (2.9 MHz), consistent with previous work[23]. In addition to the lattice itself, the circuit contains four measurement ports, visible in each corner, which are used to interrogate the lattice.

Theoretical transmission curves for 15 different disorder realizations are shown in Fig. 6c, along with a plot of the experimental transmitted power near the second harmonic frequency of the device. These theoretical curves reproduce most of the qualitative features of the data, including the onset of peaks, the location and Fano-like lineshapes of the highest-frequency peaks, and the markedly larger linewidth of the modes near 16.2 GHz which have the largest overlap with the coupling ports. This device therefore demonstrates that hyperbolic lattices can be produced on chip by using CPW resonators, and it paves the way to the study of interactions in hyperbolic space and to simulation of new models with non-constant curvature.

Because of the combination of systematic and random disorder, in practice the flat band will no longer be completely degenerate and will hybridize slightly with the rest of the spectrum. For this heptagon-kagome device, the systematic shape-dependent disorder causes the largest effects: about $0.12|t|$ for the worst shapes and about $0.07|t|$ for typical ones. Random disorder contributes at about the $0.04|t|$ level. Using graph-theoretic studies beyond the scope of the discussion here, we have have shown that the bulk gap for the heptagon-kagome lattice is about $0.4|t|$ and that the lower-lying eigenvalues seen in finite-size numerics are whispering-gallery-like edge modes which are very strongly confined to the boundary[46]. Therefore, the gapped flat band of the heptagon-kagome lattice is noticeably broadened, but is able to survive in the experimental realization. These graph-theoretic studies also revealed the existence of closely related and readily realizable lattices with gaps as large as $|t|$ for which the hierarchy of energy scales is favourable.

Conclusion

We have shown that lattices of CPW resonators can be used to produce artificial photonic materials in an effective curved space, including hyperbolic lattices which are typically prohibited as they cannot be isometrically embedded, even in three dimensions. In particular, we conducted numerical tight-binding simulations of hyperbolic analogs of the kagome lattice and demonstrated that they display a flat band

similar to that of their Euclidean counterpart. However, for the case of odd-sided polygons this band is isolated from the rest of the spectrum. We also constructed a proof-of-principle experimental device which realizes a finite section of non-interacting heptagon-kagome lattice. In addition to the curved-space lattices discussed here, this technique can be used to create a large variety of other graphs and lattices such as two-dimensional sheets with ripple distortions, Cayley trees or Cayley graphs of free products of cyclic groups.

Although our present work is purely non-interacting, interactions can be included by incorporating kinetic inductance materials to obtain a classical χ^3 nonlinearity[47,48], or by the addition of qubits to each resonator. Alternatively, it is possible to appropriate the techniques of hyperbolic metamaterials in which the equations of motion are tailored to mimic the existence of a non-trivial metric by deliberate modulation of the dielectric constant. A discrete version of the same effect[17,18] can be realized here by tailoring the hopping magnitude, providing a simple route to models of more moderate curvature and specific metrics such as the Schwarzschild solution. The promise of strong interactions in these lattices may lead to answers to questions at the interface of quantum mechanics, gravity and condensed matter physics, as lattices with these properties cannot be fabricated from actual materials.

Online content

Any methods, additional references, Nature Research reporting summaries, source data, statements of data availability and associated accession codes are available at https://doi.org/10.1038/s41586-019-1348-3.

Received: 15 March 2018; Accepted: 26 April 2019;
Published online 3 July 2019.

1. Cannon, J. W., Floyd, W. J., Kenyon, R. & Parry, W. R. in *Flavors of Geometry* **31**, 59–115 (MSRI, 1997).
2. Leonhardt, U. & Philbin, T. G. General relativity in electrical engineering. *New J. Phys.* **8**, 247 (2006).
3. Batz, S. & Peschel, U. Linear and nonlinear optics in curved space. *Phys. Rev. A* **78**, 043821 (2008).
4. Smolyaninov, I. I. & Narimanov, E. E. Metric signature transitions in optical metamaterials. *Phys. Rev. Lett.* **105**, 067402 (2010).
5. Genov, D. A., Zhang, S. & Zhang, X. Mimicking celestial mechanics in metamaterials. *Nat. Phys.* **5**, 687–692 (2009).
6. Chen, H., Miao, R.-X. & Li, M. Transformation optics that mimics the system outside a Schwarzschild black hole. *Opt. Express* **18**, 15183–15188 (2010).
7. Bekenstein, R. et al. Control of light by curved space in nanophotonic structures. *Nat. Photon.* **11**, 664–670 (2017).
8. Bekenstein, R., Schley, R., Mutzafi, M., Rotschild, C. & Segev, M. Optical simulations of gravitational effects in the Newton–Schrödinger system. *Nat. Phys.* **11**, 872–878 (2015).
9. Unruh, W. G. Experimental black-hole evaporation. *Phys. Rev. Lett.* **46**, 1351–1353 (1981).
10. Weinfurtner, S., Tedford, E. W., Penrice, M. C. J., Unruh, W. G. & Lawrence, G. A. Measurement of stimulated Hawking emission in an analogue system. *Phys. Rev. Lett.* **106**, 021302 (2011).
11. Philbin, T. G. et al. Fiber-optical analog of the event horizon. *Science* **319**, 1367–1370 (2008).
12. Steinhauer, J. Observation of quantum Hawking radiation and its entanglement in an analogue black hole. *Nat. Phys.* **12**, 959–965 (2016).
13. Carusotto, I., Fagnocchi, S., Recati, A., Balbinot, R. & Fabbri, A. Numerical observation of Hawking radiation from acoustic black holes in atomic Bose–Einstein condensates. *New J. Phys.* **10**, 103001 (2008).
14. Gerace, D. & Carusotto, I. Analog Hawking radiation from an acoustic black hole in a flowing polariton superfluid. *Phys. Rev. B* **86**, 144505 (2012).
15. Sabín, C. Mapping curved spacetimes into Dirac spinors. *Sci. Rep.* **7**, 40346 (2017).
16. Pedernales, J. S. et al. Dirac equation in (1+1)-dimensional curved spacetime and the multiphoton quantum Rabi model. *Phys. Rev. Lett.* **120**, 160403 (2018).
17. Koke, C., Noh, C. & Angelakis, D. G. Dirac equation in 2-dimensional curved spacetime, particle creation, and coupled waveguide arrays. *Ann. Phys.* **374**, 162–178 (2016).
18. Boada, O., Celi, A., Latorre, J. I. & Lewenstein, M. Dirac equation for cold atoms in artificial curved spacetimes. *New J. Phys.* **13**, 035002 (2011).
19. Houck, A. A., Türeci, H. E. & Koch, J. On-chip quantum simulation with superconducting circuits. *Nat. Phys.* **8**, 292–299 (2012).
20. Anderson, B. M., Ma, R., Owens, C., Schuster, D. I. & Simon, J. Engineering topological many-body materials in microwave cavity arrays. *Phys. Rev. X* **6**, 041043 (2016).
21. Fitzpatrick, M., Sundaresan, N. M., Li, A. C. Y., Koch, J. & Houck, A. A. Observation of a dissipative phase transition in a one-dimensional circuit QED lattice. *Phys. Rev. X* **7**, 011016 (2017).
22. Schmidt, S. & Koch, J. Circuit QED lattices: towards quantum simulation with superconducting circuits. *Ann. Phys. (Berl.)* **525**, 395–412 (2013).
23. Underwood, D. L., Shanks, W. E., Koch, J. & Houck, A. A. Low-disorder microwave cavity lattices for quantum simulation with photons. *Phys. Rev. A* **86**, 023837 (2012).
24. Coxeter, H. S. M. Regular honeycombs in hyperbolic space. In *Proc. ICM Amsterdam* **3**, 155–169 (1954).
25. Schmidt, S., Gerace, D., Houck, A. A., Blatter, G. & Türeci, H. E. Nonequilibrium delocalization-localization transition of photons in circuit quantum electrodynamics. *Phys. Rev. B* **82**, 100507 (2010).
26. Raftery, J., Sadri, D., Schmidt, S., Türeci, H. E. & Houck, A. A. Observation of a dissipation-induced classical to quantum transition. *Phys. Rev. X* **4**, 031043 (2014).
27. Woess, W. Context-free languages and random walks on groups. *Discrete Math.* **67**, 81–87 (1987).
28. Sunada, T. Group C*-algebra sand the spectrum of a periodic Schrödinger operator on a manifold. *Can. J. Math.* **44**, 180–193 (1992).
29. Floyd, W. J. & Plotnik, S. P. Growth functions on Fuchsian groups and the Euler characteristic. *Invent. Math.* **88**, 1–29 (1987).
30. Bartholdi, L. & Ceccherini-Silberstein, T. G. Growth series and random walks on some hyperbolic graphs. *Monatsh. Math.* **136**, 181–202 (2002).
31. Strichartz, R. S. Harmonic analysis as spectral theory of Laplacians. *J. Funct. Anal.* **87**, 51–148 (1989).
32. McLaughlin, J. C. *Random Walks and Convolution Operators on Free Products*. PhD thesis, New York Univ. (1986).
33. Agmon, S. Spectral theory of Schrödinger operators on Euclidean and non-Euclidean spaces. *Commun. Pure Appl. Math.* **39**, S3–S16 (1986).
34. Krioukov, D., Papadopoulos, F., Kitsak, M. & Vahdat, A. Hyperbolic geometry of complex networks. *Phys. Rev. E* **82**, 036106 (2010).
35. Boguñá, M., Papadopoulos, F. & Krioukov, D. Sustaining the Internet with hyperbolic mapping. *Nat. Commun.* **1**, 62 (2010).
36. Lipton, R. J. & Tarjan, R. E. A separator theorem for planar graphs. *SIAM J. Appl. Math.* **36**, 177–189 (1979).
37. Breuckmann, N. P. & Terhal, B. M. Constructions and noise threshold of hyperbolic surface codes. *IEEE Trans. Inf. Theory* **62**, 3731–3744 (2016).
38. Breuckmann, N. P., Vuillot, C., Campbell, E., Krishna, A. & Terhal, B. M. Hyperbolic and semi-hyperbolic surface codes for quantum storage. *Quantum Sci. Technol.* **2**, 035007 (2017).
39. Blais, A., Huang, R.-S., Wallraff, A., Girvin, S. M. & Schoelkopf, R. J. Cavity quantum electrodynamics for superconducting electrical circuits: an architecture for quantum computation. *Phys. Rev. A* **69**, 062320 (2004).
40. Koch, J. et al. Charge-insensitive qubit design derived from the Cooper pair box. *Phys. Rev. A* **76**, 042319 (2007).
41. Reagor, M. et al. Quantum memory with millisecond coherence in circuit QED. *Phys. Rev. B* **94**, 014506 (2016).
42. Ashcroft, N. W. & Mermin, N. D. *Solid State Physics* (Thomson Learning, 1976).
43. Kroto, H. W., Heath, J. R., O'Brien, S. C., Curl, R. F. & Smalley, R. E. C_{60}: buckminsterfullerene. *Nature* **318**, 162–163 (1985).
44. Bergman, D. L., Wu, C. & Balents, L. Band touching from real-space topology in frustrated hopping models. *Phys. Rev. B* **78**, 125104 (2008).
45. Leykam, D., Andreanov, A. & Flach, S. Artificial flat band systems: from lattice models to experiments. *Adv. Phys. X* **3**, 1473052 (2018).
46. Kollár, A. J., Fitzpatrick, M., Sarnak, P. & Houck, A. A. Line-graph lattices: Euclidean and non-Euclidean flat bands, and implementations in circuit quantum electrodynamics. Preprint at https://arxiv.org/abs/1902.02794 (2019).
47. Annunziata, A. J. et al. Tunable superconducting nanoinductors. *Nanotechnology* **21**, 445202 (2010).
48. Rotzinger, H. et al. Aluminium-oxide wires for superconducting high kinetic inductance circuits. *Supercond. Sci. Technol.* **30**, 025002 (2016).

Acknowledgements We thank P. Sarnak, J. Kollár, R. Bekenstein, C. Fefferman and S. Parameswaran for discussions. This work was supported by the US National Science Foundation, the Princeton Center for Complex Materials (DMR-1420541) and the Multidisciplinary University Research Initiative (MURI) (W911NF-15-1-0397).

Author contributions A.J.K. conceived of the experiment, performed numerical simulations, measured the device and prepared the manuscript. M.F. designed, fabricated and measured the device, and prepared the manuscript. A.A.H. supervised the work.

Competing interests The authors declare no competing interests.

Additional information
Extended data is available for this paper at https://doi.org/10.1038/s41586-019-1348-3.
Reprints and permissions information is available at http://www.nature.com/reprints.
Correspondence and requests for materials should be addressed to A.J.K.
Reviewer information *Nature* thanks Göran Johansson, Prof. Enrique Solano and Martin Weides for their contribution to the peer review of this work.
Publisher's note: Springer Nature remains neutral with regard to jurisdictional claims in published maps and institutional affiliations.

METHODS

CPW resonators and circuit QED lattices. The lattices in this paper are made using CPW resonators, which can easily be etched from a single layer of superconducting film. They are a planar analogue of a cylindrical coaxial cable, and consist of an electrically isolated centre pin surrounded by two ground planes on either side. Resonators are readily defined simply by removing a section of the centre pin, and the external quality factor is set by this capacitive gap. By microfabrication standards they are fairly large, several millimetres in length, so they are typically fabricated with meanders to make them more compact, as seen in Fig. 1b–d.

Lattices, such as those shown in Fig. 1a and Fig. 6b, are formed by connecting many resonators together end to end[22,23]. The strength of the coupling is determined by the capacitance at the junction where the centre pins converge. The hopping rate is naturally negative, and as a result, these systems exhibit band structures that are inverted from what is typically found in actual solid-state systems, with rapidly oscillating Bloch waves at the low-energy end of the spectrum. Larger coordination numbers than three are possible, but the circuit layout tends to produce considerable next-nearest-neighbour hopping, which greatly complicates the description of the network and will not be discussed here.

When two resonators are coupled together, their modes hybridize and produce bonding and antibonding configurations. Which of these is lower in frequency is determined by the energetics of the electric field distribution given the type of coupling element. When the resonators are laid out in a periodic lattice, the circuit naturally maps to a tight-binding model of a 2D crystalline solid. The type of lattice (square, kagome or other) is determined by how the resonators are connected together, and the frequency of the resonator maps to the atomic binding energy of the conduction band. The capacitive coupling between resonators can be expressed as a nearest-neighbour hopping rate, t. The sign of the matrix element must be chosen to yield the correct physical behaviour given the sign of the on-site wavefunctions.

The eigenmodes of the CPW resonators are standing waves with an antinode of the voltage at each end of the cavity. Quantum computing applications typically use the fundamental, half-wave, mode. However, when studying network or lattice physics, the inherent asymmetry of the half-wave mode complicates the sign of the hopping rates. In many cases, this minus sign can be removed by a local gauge transformation that redefines positive and negative on alternating sites[22]. However, for many of the hyperbolic lattices considered here, this gauge transformation is not possible, and it is impossible to consistently define all the hopping rates with the same sign. This complicates the mathematical description and, in some cases, induces additional geometric frustration. The second-harmonic, or full-wave, mode is symmetric and does not have this sign complication. In the main text, we therefore restrict the discussion to full-wave modes, and all results, unless explicitly stated, will refer to this case.

Regardless of whether the on-site wavefunction is even or odd, it is energetically favourable for the voltages on either side of the coupling capacitors connecting the resonators to be of opposite sign. Circuit QED lattices therefore exhibit band structures that are inverted from what is found in typical solid-state systems, with rapidly oscillating Bloch waves at the low-energy end of the spectrum. For full-wave modes, this physics can be captured by a standard tight-binding model with negative t. For half-wave modes, a global definition of the sign of t may no longer be possible, and care must be taken[22,42]. We proceed by defining an orientation for each resonator and arbitrarily designate one end of each resonator 'positive' and one end 'negative'. For the tight-binding model to be physical, the sign of t must be consistent with the designated orientation and always favour opposite voltages on either side of the coupling capacitors. Therefore, $t < 0$ when it describes hopping between two ends of the same sign and $t > 0$ when describing hopping between two ends of different sign.

As hinted above, the choice of the orientation of each half-wave resonator is arbitrary and merely a bookkeeping convention. Some choices are, of course, more convenient and illustrative than others. For some layout lattices, for example square or hexagonal, the orientation of each resonator can be chosen consistently such that all hopping matrix elements are negative, even for half-wave modes[22]. In these cases, the asymmetry of the on-site wavefunction can be gauged away by this judicious choice of orientations, and the half-wave tight-binding model is isomorphic to the version with even on-site wavefunctions, in much the same way that the magnon spectrum of an unfrustrated antiferromagnet is identical to that of the corresponding ferromagnet. However, if the layout lattice contains plaquettes with an odd number of sides, then an orientation that fixes the sign of the hopping matrix elements cannot generally be found. Compared with their full-wave counterparts, these tight-binding models exhibit additional geometric frustration due to the phase windings forced by the half-wave mode function.

This effect can most easily be seen by considering the maximally excited state of a kagome-like layout lattice, which has eigenvalue $4|t|$. The defining features of this state are uniform probability of occupation of all the sites and equal voltages on either side of all coupling capacitors. For full-wave modes, both of these conditions are easily satisfied by uniform occupation of all cavities with a single phase. For half-wave modes, this is not the case. Consider a single layout plaquette of the lattice and define the orientations such that going from the positive to the negative end of a resonator corresponds to moving clockwise around the plaquette. To maintain equal voltages on both sides of all coupling capacitors using half-wave modes, the sign of the on-site wavefunction must alternate on neighbouring sites, which cannot be done consistently on a plaquette with an odd number of sides.

Hyperbolic kagome lattices made from even-sided polygons are free of this effect, and the asymmetry of the half-wave mode function can always be gauged away. Kagome-like lattices made from odd-sided polygons, on the other hand, are frustrated. Remarkably, the flat band is immune to these frustration effects because it is spanned by states that consist of loops with an even number of edges, such as the one shown in Extended Data Fig. 2g. The dispersive bands above $E = -2|t|$, however, are affected, and the spectral gap that isolates the flat band in the full-wave case disappears from the half-wave model.

Device characterization. The device was fabricated using photolithography and reactive ion etching to pattern CPW resonators in a 200 nm film of niobium on a 500 μm sapphire substrate. The resonators were 7.5 mm long with a target fundamental resonance frequency of 8 GHz and a second harmonic of 16 GHz, and respective hopping rates of −70 MHz and −140 MHz. All couplers in the device are three-way couplers like the one shown in Fig. 1e, including in the outermost ring, where an outgoing edge of the infinite layout graph has often been removed. In these cases, the missing resonator is replaced with a high-frequency $\lambda/4$ stub resonator. These stubs are too far detuned to enter into the effective tight-binding model for the device, but they ensure uniform capacitive loading of all the resonators and prevent reduced coupling capacitances from renormalizing the on-site energies of the resonators at the edge of the device. Four of these stub resonators are replaced with transmission lines leading away from the device to provide the external coupling ports visible in each corner of Fig. 6b. Initially, the length of all resonators was designed constant throughout the device by varying the number and extent of the meanders, to compensate for the required differences in the distance between the end points of each resonator. However, it was found that initially there were small residual differences in frequency (up to 0.37% or 30 MHz) for resonators of different shapes, due to parasitic effects.

To compensate for this, each unique resonator shape was fabricated on different chips and measured individually. Then, incremental changes were made to the total length to eliminate the parasitic frequency errors. The u-shaped resonators on the outer ring were the most numerous type, so all other resonators were adjusted to match their measured frequency of 7.99 GHz. The test resonators used to compensate for the resonator frequency offsets also provided an independent measure of intrinsic disorder levels. Within a single fabrication run, resonators of the same geometry had variations in their frequencies of 0.036% (2.9 MHz), which is consistent with previous results[23]. Compensation for the systematic offsets between shapes was limited by the intrinsic reproducibility and variations between fabrication runs. For most of the resonator shapes, the systematic disorder causes the on-site energies to fall within a window of 0.13% (10 MHz). However, the middle and outer rings of resonators proved more sensitive to fabrication variations, presumably owing to parasitic capacitances in the long parallel straight sections of the waveguides. Systematic offsets in these resonators could be eliminated to the 0.19% (15 MHz) level.

The final, disorder-compensated, device was mounted in a microwave printed circuit board using indium seals and aluminium wire bonds. The device was anchored to the base plate of a dilution refrigerator, and the input to the lattice was provided using a high-frequency microwave generator. The fundamental modes of the device constitute a heptagon-kagome lattice with mixed sign of the hopping matrix elements. We therefore measure the symmetric second-harmonic modes near 16 GHz using a cryogenic HEMT amplifier and heterodyne down-conversion. The connectivity and on-site energies of the device were verified using theoretical reconstructions of expected transmission spectra discussed below.

Transmission simulations. To simulate the transmission properties of the device, we use finite-size tight-binding calculations. We input the average resonator frequency, the hopping rate and the systematic offsets in the on-site energies, allowing a different average value for each azimuthal ring and each of the two sets of radial resonators. To further match the device, we introduce disorder in the device parameters at the level given by the individual resonator tests. After numerical diagonalization, we obtain the frequency and wavefunction of each eigenmode of the lattice. Assuming a typical half-width at half-maximum of 1.4 MHz, we generate a Lorentzian resonance profile for each mode, centred about its eigenenergy. We then compute the level of mode matching between the eigenmodes and the input and output ports using the numerical wavefunctions. To calculate the transmitted electric field versus probe frequency, we sum the transmission through all 140 eigenmodes, weighted by their Lorentzian line shapes and spatial mode matching. Finally, we produce ensembles of different random disorder realizations.

In the frequency range of 15–17 GHz, the main limitation to measurement is leakage transmission through the PCB housing around the device, which gives rise to a frequency-dependent coherent background in all transmission measurements with variations on the scale of 50–100 MHz. Unfortunately, this background is extremely sensitive to the exact microwave boundary conditions around the device and cannot be measured independently of the device. However, it is considerably more broadband than the device transmission peaks. We therefore use the experimental data to gain an empirical estimate of this background signal. Using a Gaussian convolution filter, we remove the components of the amplitude signal which vary rapidly with probe frequency. The resulting filtered signal constitutes an experimental measure of the leakage power. The phase of the device transmission swings by many multiples of 2π, making it impossible to unwrap and perform a similar reconstruction of the phase of the leakage signal. We therefore estimate the leakage electric field by taking the square root of the leakage power and neglect the slow phase variations that are present in the actual device.

Adding this empirical background to the theoretical electric fields obtained from numerical diagonalisation yields an ensemble of simulated transmission curves. Figure 6c shows the experimental transmission curve in blue and a best-fit ensemble of 15 theoretical simulations in red. These theoretical curves reproduce most of the qualitative features of the data including: the onset of peaks, the location and Fano-like lineshapes of the highest frequency peaks, and the markedly larger linewidth of the modes near 16.2 GHz, which have the largest overlap with the coupling ports. The theoretically estimated on-site energies are within estimated error. The two outer rings are slight outliers with systematic offsets of -7 MHz and $+15$ MHz at the fundamental modes, whereas all the other shapes lie within ± 5 MHz. The theoretically estimated hopping rate of -136.2 MHz is consistent with software simulations.

Curved-space tight-binding models. No hyperbolic equivalent of Bloch theory currently exists, and there is no known general procedure for calculating band structures in either the nearly-free-electron or tight-binding limits. Specialized methods are known for the cases of trees[49,50] but fail if there are any closed loops, except in the special case of Cayley graphs of the free products of cyclic groups[32]. The only universal method is numerical diagonalization of the hopping Hamiltonian. This is a brute-force method which yields a list of eigenvectors and eigenvalues, but no classification of eigenstates by a momentum quantum number. It therefore cannot be used to directly obtain the dispersion relations. Instead, it is more useful as a measure of the energy spectrum and the density of states.

Numerical diagonalization studies of finite-size tight-binding models of the heptagon-kagome lattice were conducted for a series of system sizes, starting with a smallest simulation consisting of a central layout heptagon and one shell of nearest-neighbour plaquettes. We compute the effective lattice of this finite layout, neglecting all links to sites outside the current system size. Larger systems are created iteratively by adding successive shells of nearest-neighbour layout polygons to the edge of the smaller simulations and recomputing the effective lattice.

Numerical eigenenergy spectra for a series of system sizes are shown in Extended Data Fig. 1. The flat band is clearly visible even for the smallest simulation with only one shell of neighbouring polygons. The spectral gap between the flat band and the rest of the spectrum is already present but not readily distinguishable from the finite-size-induced gaps at higher energy. Within the size of simulation currently possible, the higher-lying gaps all close progressively with increasing system size, and it remains unclear whether any of them also remain open at infinite size. Because the spectral gap between the flat band and the rest of the energy spectrum is readily visible for systems with two or more layers of neighbour polygons, our physical device, shown in Fig. 6, was constructed at this depth.

Colour plots of selected numerical eigenstates from a three-shell simulation of the heptagon-kagome lattice are shown in Extended Data Fig. 2. Owing to the negative hopping amplitude, the uniform-phase configuration typically associated with the ground state of a lattice is, in fact, the highest excited state, shown in Extended Data Fig. 2a. Additionally, it exhibits a radial amplitude modulation due to confinement from the missing links beyond the edge of the sample, which constitute an effective hard-wall potential. The next eigenstates down (Extended Data Fig. 2b, c) bear a striking resemblance to the Laguerre-type 0, 1 and 0, 2 modes of a Euclidean harmonic oscillator or a particle in a cylindrical box. The qualitative similarity persists for many modes throughout the spectrum, such as the one shown in Extended Data Fig. 2d which resembles a Laguerre 4, 7 mode.

Conversely, the eigenstates also show several features that are strikingly different from the Euclidean case. Because of the hyperbolic nature of the lattice, a macroscopic fraction of the lattice sites are in the outermost ring, and there are a relatively large number of eigenstates like the one in Extended Data Fig. 2e which reside primarily at the edge of the system. Another intriguing feature is the existence of states like the one in Extended Data Fig. 2f, which display azimuthal amplitude and phase modulation with different periods.

A flat-band eigenstate is shown in Extended Data Fig. 2g. The analogous state in the kagome lattice encircles a single hexagonal plaquette, but this type of behaviour is not possible in a hyperbolic kagome-like lattice formed with odd-sided polygons because the sign flips cannot be consistently maintained. Therefore, the flat-band state in the heptagon kagome lattice (or any $(2n+1)$-gon kagome lattice) consists of a single loop across two plaquettes in which the phase flips by π between every neighbouring pair of sites. It is a localized eigenstate which is protected from hopping by destructive interference in the triangular plaquettes which border the loop. As this state has compact support, translations of it are orthogonal and form a degenerate manifold of states whose multiplicity is proportional to the system size.

Lattice curvatures. Compared with spherical or hyperbolic space, familiar Euclidean space is unique in that there is no intrinsic length scale. In particular, polygons have the same internal angles, regardless of size. Therefore, any Euclidean tiling can be scaled up or down in size and remain unchanged. This is not true in spherical or hyperbolic space where there is a natural length scale R that is set by the Gaussian curvature $K = \pm\, 1/R^2$ [51]. Space with positive (spherical) curvature is effectively smaller than flat space. For example the circumference of a disk of radius r is $2\pi\, R \sin(r/R) < 2\pi\, r$. Hyperbolic space with negative curvature is the opposite. It is larger than flat space, and the circumference of a disk of radius r is $2\pi\, R \sinh(r/R) > 2\pi\, r$.

In both cases, the shape of a polygon depends on its size relative to this length scale[1,21]. For example, consider a triangle on the surface of a sphere which has one vertex at the north pole and the other two on the equator separated by $\pi/2$ longitudinally. The total internal angle of this triangle is $3\pi/2$ (each angle is $\pi/2$), but if it is reduced in size until it is much smaller than the radius of curvature of the sphere, it tends to a Euclidean triangle with a total internal angle of π. Tiles in spherical space therefore get 'fatter' as they increase in size and can cover gaps left between Euclidean tiles of the same shape. Hyperbolic polygons, however, have smaller internal angles at their vertices than their Euclidean counterparts. Therefore, hyperbolic tilings are precisely those for which the tiles would overlap if drawn according to Euclidean geometry. (See Fig. 3). As hyperbolic polygons become larger and larger, their internal angles decrease progressively, and they become 'pointier'.

Because of this size-dependent geometry, whether or not a set of tiles can form a valid lattice in curved space depends on their size. The polygons must be precisely big enough that the tiles fit exactly. Increasing the size of the polygons further will cause gaps or overlaps to appear between the tiles, depending on the sign of the curvature. Therefore, for fixed curvature, each non-Euclidean lattice can only exist for a specific tile size. Conversely, each lattice can be thought of as having an intrinsic curvature given by the required ratio of inter-site spacing and R.

To determine these curvatures for the hyperbolic tilings considered here, we make use of the Poincaré disk model conformal mapping of the 2D hyperbolic plane with curvature -1 onto the Euclidean unit disk[1]. For concreteness, we consider only hyperbolic tilings that are generalizations of graphene to polygons with a larger number of sides. These are precisely those that produce kagome-like effective models. The layout tiling will exist when a hyperoblic n-gon can be produced which is bounded by geodesics and whose hyperbolic internal angle is $2\pi/3$, allowing copies of it to be tiled in a graphene-like way with three tiles meeting at every vertex. Because the Poincaré disk model is a conformal model that preserves angles, it suffices to determine the polygon size that results in an internal angle of $2\pi/3$ when drawn in the unit disk. The geodesics of the Poincaré disk model are circles that intersect the unit disk at an angle of $\pi/2$ and the metric is known analytically, so the radius and edge length of the tile required to form the layout lattice can be readily determined. The corresponding inter-site spacing for the effective lattice is determined by computing the distance between the midpoints of the edges of the layout polygon.

For the heptagon-graphene layout lattice, the inter-site spacing is determined as $0.566R$ (ref. [21]), and the curvature of the resulting heptagon-kagome effective lattice is slightly weaker with an inter-site spacing of $0.492R$. Lattice spacing and Poincaré disk model plots of a series of graphene- and kagome-like lattices are shown in Extended Data Fig. 3. The ratio of the lattice spacing to R increases with increasing number of sides of the layout polygon because the corresponding attempt at a Euclidean tiling has more and more overlap that needs to be removed by increasing the size of the tiles. This is clearly visible in the plots, as the polygon at the origin occupies a larger and larger fraction of the unit disk. In fact, the heptagon-graphene tiling has the smallest ratio of lattice spacing to curvature of any tiling of the hyperbolic plane by a single polygon, regardless of vertex coordination number. Correspondingly, the heptagon-kagome has the weakest curvature of all the resulting effective lattices, making this pair natural entry points to the study of hyperbolic lattices.

Data availability

The data and codes are available from the corresponding author upon reasonable request.

49. Kesten, H. Symmetric random walks on groups. *Trans. Am. Math. Soc.* **92**, 336–354 (1959).
50. Chen, M. S., Onsager, L., Bonner, J. & Nagle, J. Hopping of ions in ice. *J. Chem. Phys.* **60**, 405–419 (1974).
51. Carroll, S. M. Lecture notes on general relativity. Preprint at https://arxiv.org/abs/gr-qc/9712019 (1997).
52. Dunham, D., Lindgren, J. & Witte, D. Creating repeating hyperbolic patterns. *Comput. Graph.* **15**, 215–223 (1981).
53. Adcock, B. M., Jones, K. C., Reiter, C. A. & Vislocky, L. M. Iterated function systems with symmetry in the hyperbolic plane. *Comput. Graph.* **24**, 791–796 (2000).

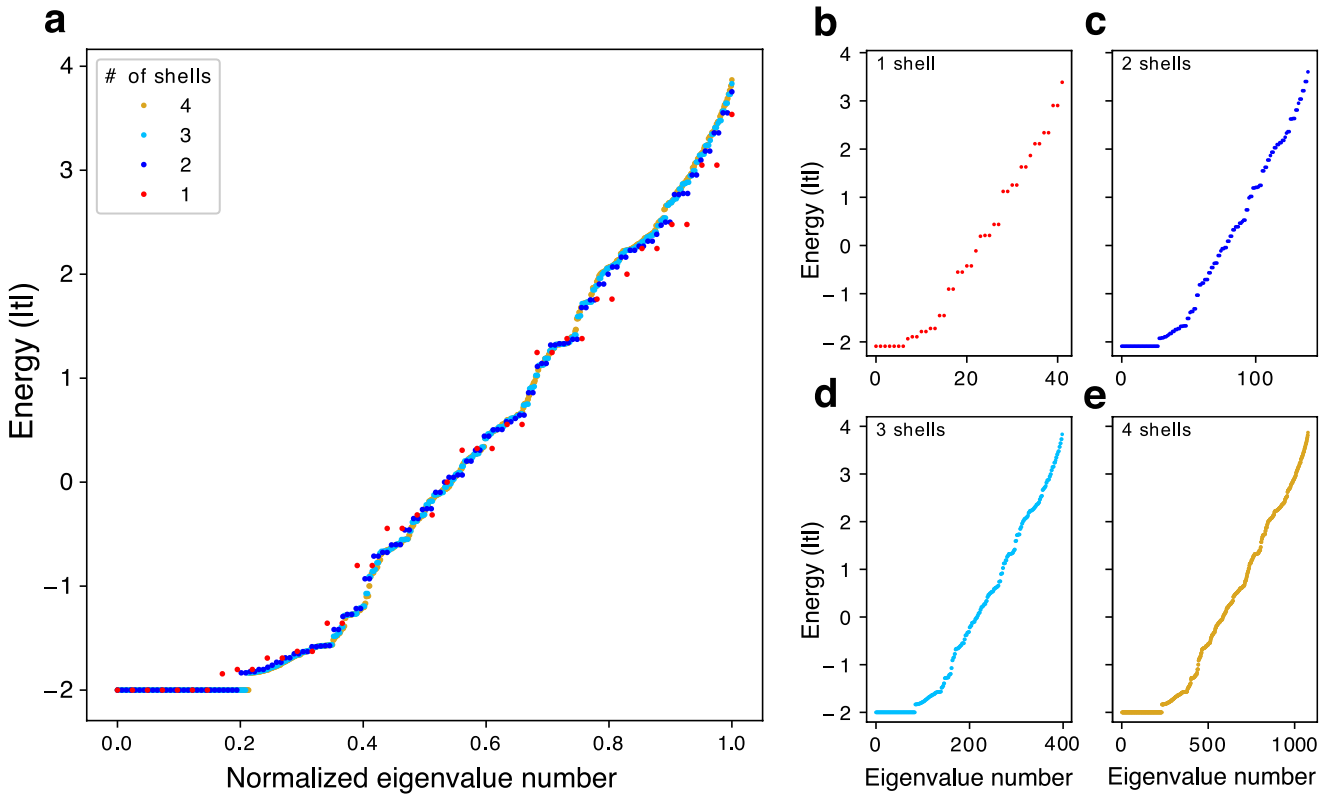

Extended Data Fig. 1 | System-size effects. a, Numerical eigenenergy spectra for the heptagon-kagome lattice versus system size. The smallest layout tiling consists of a central heptagon and a shell of seven immediate neighbours (one shell). Each successive tiling includes another shell of immediate neighbours of the previous one. The spectra are plotted for one (red), two (blue), three (cyan) and four (gold) shells of neighbours. **b**–**e**, The results for each individual system size. The density of states converges rapidly with number of shells despite relatively small system sizes and effective hard-wall confinement. The theoretical plots elsewhere in this paper are from three-shell simulations. The experimental device consists of two shells.

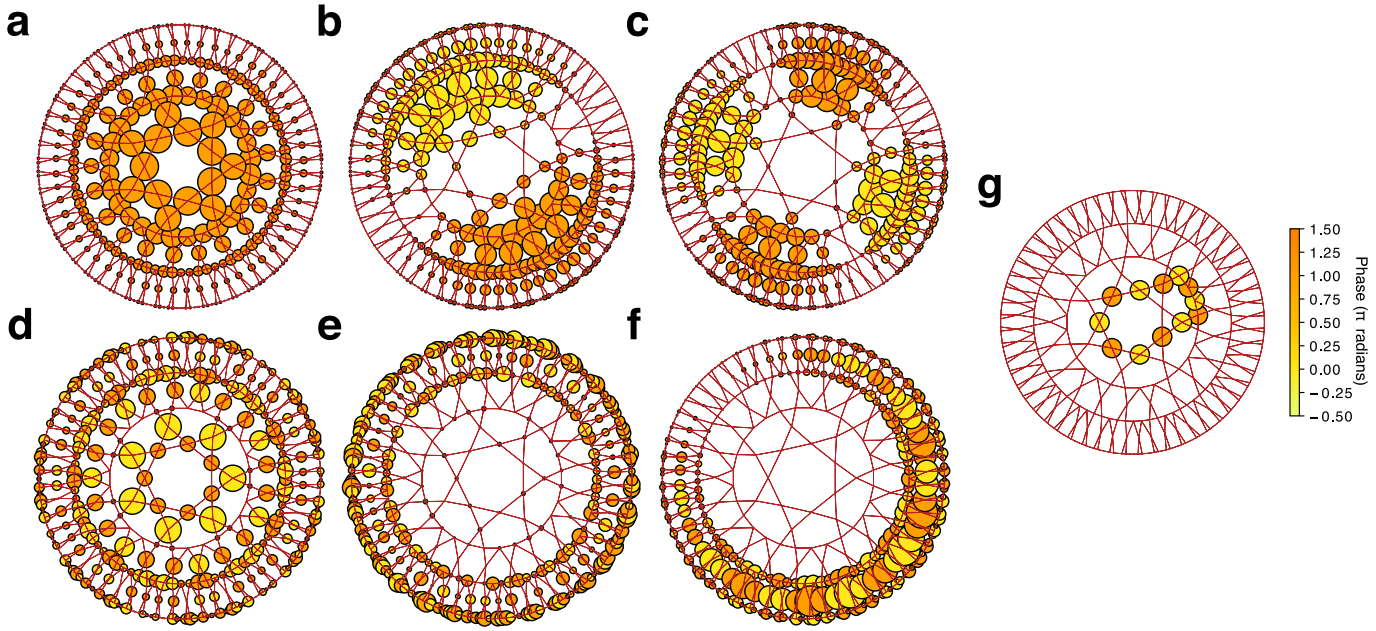

Extended Data Fig. 2 | Colour plots of selected numerical eigenstates of three shells of the heptagon-kagome lattice. States are ordered from highest to lowest energy, and are plotted by placing a circle on each lattice site of the effective lattice. The size of the circle indicates the amplitude of the state on that site, and the colour its phase. **a**, The maximally excited state. This state is uniform in phase, but its amplitude varies radially owing to the effective confinement from the missing links at the boundary of the simulation. **b**, **c**, Examples of the two next-highest states. They bear a striking resemblance to Laguerre–Gaussian or particle-in-a-cylindrical-box modes found in flat Euclidean space. **d**–**f**, Selected intermediate excited states. Notice that the state in **f** shows both amplitude and phase modulation in the azimuthal direction, with independent periods. **g**, The localized eigenstate of compact support that forms the flat band.

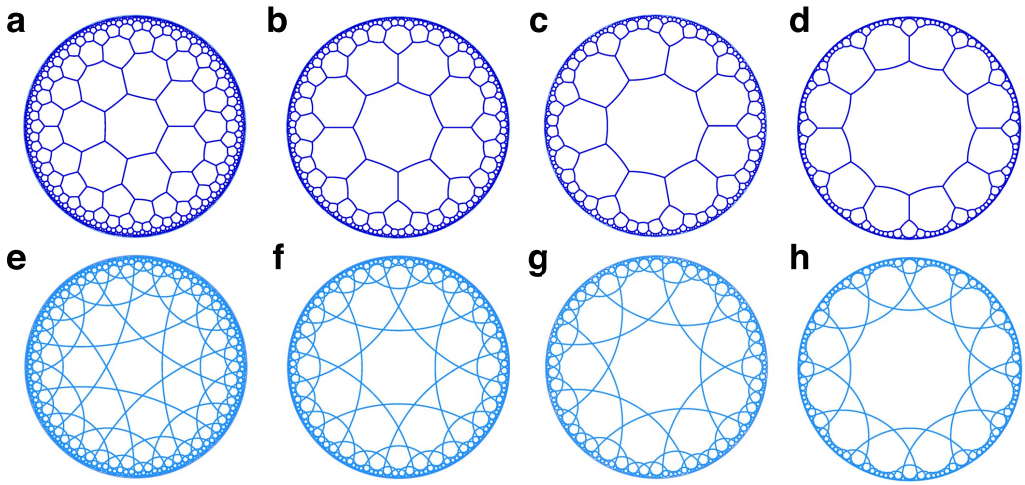

i

Tiling Polygon (n)	Lattice Constant	Medial Lattice Constant
7	0.566	0.492
8	0.727	0.633
9	0.819	0.714
10	0.879	0.767
11	0.921	0.804
12	0.952	0.831

Extended Data Fig. 3 | Poincaré-disk-model[1,52,53] conformal projections of hyperbolic lattices. a–**d**, Graphene-like lattices formed from heptagons, octagons, nonagons and dodecagons, respectively. **e**–**h**, The corresponding kagome-like effective lattices that arise when **a**–**d** are used as the layout lattice. **i**, A table of inter-site spacings for graphene-like hyperbolic layout lattices and their medial lattices, the kagome-like effective lattices. All distances are given in terms of the curvature length $R = 1/\sqrt{|K|}$. As the number of sides of the layout polygon increases, the intrinsic curvature of the tiling also grows, and the polygons become markedly larger.